

Highly Sensitive Detection of Processes Occurring Inside Nanoporous Anodic Alumina Templates: A Waveguide Optical Study

King Hang Aaron Lau,[†] Le-Shon Tan,[†] Kaoru Tamada,[‡] Melissa S. Sander,[†] and Wolfgang Knoll^{*,§}

Institute of Materials Research and Engineering, 3 Research Link, Singapore 117602, and Departments of Chemistry and of Materials Science, National University of Singapore, 10 Science Drive 4, Singapore 117543

Received: January 12, 2004; In Final Form: April 12, 2004

We have applied nanoporous anodic alumina films as planar optical waveguides and studied changes in the effective dielectric constants of these thin films due to various processes occurring in the pores. We demonstrate the potential of the porous anodic alumina waveguide for high sensitivity (bio-) chemical sensing with bovine serum albumin adsorption and desorption at various pH values, with subangstrom sensitivity in the effective thickness of protein adsorbed. We also monitored pore widening (alumina dissolution) with subangstrom sensitivity, which is conceptually the reverse of detecting conformal film deposition on pore surfaces. Furthermore, we monitored the exchange of pore-filling media between phosphate buffer solution and ethanol, which produces qualitatively the same response as complete pore filling with other materials by various deposition techniques. Thus porous anodic alumina films may be employed simultaneously as deposition templates and as highly sensitive detectors of processes within the pores.

I. Introduction

Porous anodic alumina films have attracted great attention in the areas of nanoscience and engineering due to their well-ordered, densely packed, nanoscale pore structure that naturally forms when aluminum films are anodized in an acidic electrolyte. These pores run straight through the film thickness, are parallel to each other, and are in the range of 10^1 to 10^2 nm in diameter. Research has focused on using porous anodic alumina (PAA) films as templates for fabricating nanoarrays of particles and nanowires of multifarious materials.^{1–5} Interest has also been expressed in their use as biomimetic scaffolds for the self-assembly of lipid membranes,^{6,7} and they have been patterned using photolithography methods for micro-electro-mechanical systems (MEMS).⁸ Excellent hexagonal pore ordering is possible through 2-step anodization⁹ or by imprinting the initial Al surface with a mold.¹⁰ The voltage and the acid electrolyte used in anodizing the aluminum determine the pore diameter and spacing, while acid etching fine-tunes the pore diameter through pore widening.^{11,12}

In this report, we apply PAA films as optical waveguides and demonstrate the monitoring of processes occurring inside the pores. Thus PAA films may be employed simultaneously as a deposition template or scaffold, as well as an in situ monitor of those processes. Very high sensitivity in the PAA sensor is possible due to the presence of a large internal surface sensitive to external stimuli (more than an order of magnitude increase in surface area compared with a flat surface for films considered in this study) and to the precise conditions necessary for guiding confined optical modes. In addition, the ability to functionalize

the alumina surface for specific (bio-) molecular detection through, for example, biotin and amine coupled silane molecules^{6,13} can confer tailored chemical specificity for sensing surface reactions (molecule-specific detection will be detailed in a later account.)

The optical behavior of the composite pore–alumina layer can be described by effective dielectric constants (ϵ_{eff}) when the pore diameter is controlled to $<1/10$ of the wavelength of the guided light.¹⁴ This is easily achieved with proper film processing and with common laboratory lasers. ϵ_{eff} values have been modeled^{1,14,15} and measured for both air- and metal-filled pores,^{1,16} and a polymer-filled PAA channel waveguide has also been demonstrated.¹⁷ When a PAA film is placed on a substrate, the pores are open to the external environment at the top and ϵ_{eff} can be changed at will by filling the pores with different media, which is detected as a change in the wave-guiding conditions and constitutes the principle of operation of the PAA sensor. For experimental simplicity, prism coupled optical waveguide spectroscopy¹⁸ was used to measure ϵ_{eff} of the PAA waveguide. However, it is emphasized that other setups such as channel waveguides and grating or end-fire coupling schemes can be employed to suit the experimental environment.

We present three examples to illustrate the operation and sensitivity of the PAA sensor. First, we examine the complete exchange of the pore material by immersing the PAA waveguide in phosphate buffer solution (PBS) and then in ethanol. PBS and ethanol were chosen because of their importance in biorelated experiments. This experiment also illustrates how the sensor distinguishes changes in film dielectric properties from a change in the surrounding media. In addition, substituting one liquid with another in the pores is analogous to complete pore filling with other materials such as metal or semiconductor by deposition into the template, in which case a different set of material-specific dielectric constants are involved. In the second experiment, we illustrate kinetic tracking of fabrication processes by monitoring pore widening, which is a key step in controlling the pore diameter. In terms of sensor response, the removal of

* To whom correspondence should be addressed: knoll@mpip-mainz.mpg.de.

[†] Institute of Materials Research and Engineering.

[‡] Present address: Bio-Photonics Group, Photonics Research Institute, National Institute of Advanced Industrial Science and Technology (AIST), Tsukuba, Ibaraki, 305-8565 Japan.

[§] Present address: Max-Planck-Institut für Polymerforschung, Ackermannweg 10, 55128 Mainz, Germany.

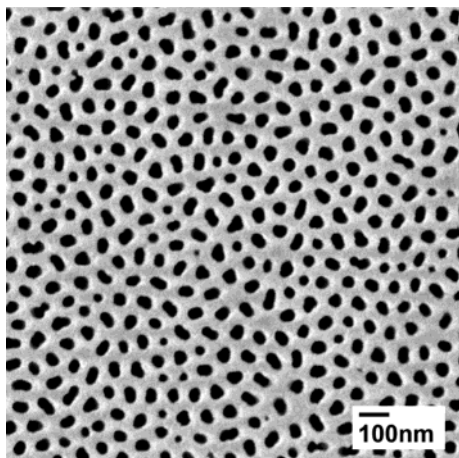


Figure 1. Typical scanning electron micrograph of a porous anodic alumina film (top view).

a layer of material is simply the reverse of conformal deposition processes that coat the film and pore surfaces and can be just as sensitively monitored. Thus conformal deposition processes such as atomic layer deposition¹⁹ and layer-by-layer growth²⁰ with PAA templates may potentially be directly analyzed in situ. Last, bovine serum albumin (BSA) adsorption and desorption at various pH on the porous alumina surface are demonstrated. BSA physisorption does not exceed a monolayer and its kinetics and equilibrium behavior have been well-characterized for alumina particle surfaces,^{21–24} as well as for a range of other surfaces.^{21,25,26} These reports in the literature form a basis for comparison and verification of the utility of the PAA film as a biomolecular sensor.

II. Experimental Section

1. Materials and SEM Characterization. Ethanol (min 99%) was purchased from Merck KGaA, Darmstadt, Singapore. Samples of 5 mM PBS of different pH values were prepared by dissolving appropriate amounts of sodium hydroxide, disodium hydrogen phosphate, sodium dihydrogen phosphate monohydrate, and 85% orthophosphoric acid (98% pure, APS Ajax Finechem) in deionized water (18.2 M Ω ·cm). All inorganic crystals were purchased from Merck KGaA, Darmstadt, Singapore (min 99%). Bovine Serum Albumin (66 kDa, Fraction V, min. 96%, pH 7) was purchased from Sigma-Aldrich Co. and was dissolved in PBS as specified above at a concentration of 50 μ M. A digital pH meter (Fisher Scientific AR 50) with uncertainty of ± 0.1 between calibrations was used for all solution preparations.

The pore structure was visualized with field emission scanning electron microscopy (JEOL JSM-6700F) at an acceleration voltage of 5 kV (Figure 1.) Samples were carbon coated (Emitech K950X) to minimize charging artifacts. Pore diameter and spacing were determined by software-assisted analysis (Scion Image, Scion Corporation; Adobe Photoshop.)

2. Optical Waveguide Spectroscopy (OWS). We performed OWS based on the Kretschmann prism coupling technique¹⁸ (Figure 2). Briefly, a thin gold coupling gap layer and aluminum were successively deposited on glass substrates index matched to the coupling prism. The aluminum was then anodized to form a PAA film (described below) before the substrate was mounted to the prism base with index matching oil. The glass prism and substrate thus form an optically contiguous medium. A $\lambda = 632.8$ nm laser was used and a polarizer selected for either p- or s-polarization. With the coupling gap layer and PAA film

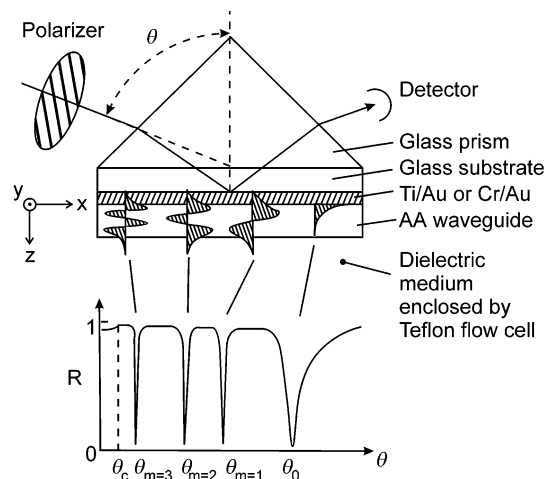


Figure 2. Schematic of the optical waveguide spectroscopy setup and of the idealized field distributions of several guided modes. Excitation of the surface plasmon and waveguide modes are observed as very sharp dips when reflectivity (R) is measured as a function of the angle of incidence (θ).

mounted on the prism assembly, the dielectric medium/environment surrounding the film naturally operated as the top cladding. We also clamped a Teflon flow cell onto the exposed film to inject and extract the desired dielectric medium/reagents.

To observe optical waveguide modes, reflectivity (R) was measured as a function of angle of incidence, θ . Both TE and TM modes (corresponding to s- and p-polarizations, respectively) can be excited in the PAA waveguide. In Figure 2, θ_c is the critical angle for total internal reflection and at angles above θ_c , guided modes can be observed as very sharp minima, indexed according to the number of nodes in their field distributions (e.g. $m = 0, 1$, etc.). The angles of these modes are completely dictated by the dielectric functions (ϵ) and thicknesses (h) of the waveguide layers, i.e., the glass layer, the coupling gap metal layer, the PAA film, and the top cladding/dielectric medium. The ϵ of the metal coupling layer was determined separately from surface plasmon measurements with the same setup¹⁸ before aluminum deposition. ϵ_{medium} was independently determined by θ_c and ϵ_{glass} has been tightly controlled by the manufacturer. As for the PAA film, the pore structure dictates that one of the principal axes of the dielectric function is parallel to the pore direction (normal to the film surface), and two are parallel to the film surface, indicated by $\epsilon_{\text{eff}} = \{\epsilon_x, \epsilon_y, \epsilon_z\}$. From Figure 1, we see that the pore distribution in the plane of the film is fairly isotropic and long-range order is weak, thus $\epsilon_x = \epsilon_y$. Therefore, only three parameters, ϵ_x , ϵ_z , and h_{PAA} , need be determined from the p-pol and s-pol mode spectra to characterize the sensor response. Although a surface plasmon resonance (SPR) mode is also expected under p-polarization ($m = 0$), the grazing angles necessary to excite this SPR in the present setup preclude its use for characterization purposes. Therefore, we have chosen $h_{\text{PAA}} \sim 1 \mu\text{m}$ such that at least two waveguide modes are always observed in R vs θ measurements of both polarizations, yielding independent information on ϵ_x , ϵ_z , and h_{PAA} with a degree of redundancy.

Experimentally, Fresnel calculations were compared with measurements to obtain the best-fit dielectric constants and layer thicknesses.¹⁸ Such calculations assume infinite layers with perfect interfaces and generate impressive agreement with data, especially with layered assemblies comprised of atomically or molecularly smooth surfaces such as mica films²⁷ or Langmuir–Blodgett assembled layers.²⁸ In the case of PAA films, the

distribution in pore diameter and surface roughness are expected to break up spatial coherence in waveguide coupling conditions over probed areas of $\sim 1 \text{ mm}^2$ corresponding to the width of the incident laser beam. These effects cause the coupling dips to broaden and decrease in amplitude in the data compared with calculated curves.

For following the kinetics of an experiment, the angle at which a reflectivity minimum characterizes a waveguide mode is tracked with in-house instrumentation. Angular resolution better than 0.005° is obtained.

3. Fabrication of Alumina Films on LaSFN9 Substrates.

LaSFN9 glass substrates (Hellma Optik, GmbH) were cut into $25 \text{ mm} \times 20 \text{ mm}$ pieces and ultrasonically cleaned in 2% Hellmanex solution (Hellma Optik, GmbH) followed by a final rinse in absolute ethanol. To ensure adhesion to the substrate, first a $\sim 3 \text{ nm}$ Cr or Ti film was deposited onto the substrate, then $\sim 46 \text{ nm}$ Au and $\sim 1 \mu\text{m}$ Al (99.9999% Alfa Aesar) were deposited. Al was deposited by electron beam evaporation (Edwards, Auto306). Ti/Au was also deposited by electron beam evaporation while Cr/Au was deposited by thermal evaporation (R-DEC Co., Ltd., Japan). To anodize the Al film, the edges of the samples were first coated with nail polish to protect them from the solution, and the sample was placed in a beaker of 0.3 M oxalic acid solution at $2\text{--}5^\circ\text{C}$ opposite a Pt mesh counter electrode. The Al was anodized at a constant potential of 40 V. When anodization was nearly complete (after 30 min), there was a distinct color change in the sample and a change in the current. To ensure that the film was completely anodized, the anodization was allowed to proceed 90–120 s past the color change. After complete anodization, the pores were widened by immersing the samples in 5 wt % of H_3PO_4 for 30 min. The PAA thus formed is stable in the ambient, and X-ray crystallography and thermogravimetric studies have confirmed that the anodization process completely oxidizes the original aluminum into an amorphous form, while annealing above 830°C induces formation of crystalline phases.²⁹

4. BSA Adsorption and Desorption. BSA adsorption proceeded in the pH range of 3.8–7.4. Before each adsorption, the flow cell was infused with PBS at the chosen pH and a R vs θ measurement was taken. The buffer was then exchanged with BSA solution and the PAA waveguide was left immersed in the BSA solution for a specific amount of time while the adsorption kinetics (coupling angle shift) were tracked. To stop the adsorption process, pure buffer at the same pH was exchanged into the flow cell. Another R vs θ measurement was taken before desorption was carried out with PBS at pH 8.5 for another specific period of time. Desorption was stopped by exchanging the cell with PBS at the pH chosen for the next adsorption–desorption cycle. Both alkali^{22,30} and acid elution³¹ are effective in desorbing BSA. However, significant pore widening occurs below pH 3.8 and above pH 8.5. No pore widening was observed for pH 5.0 to 7.4 and acceptably slow etching at a rate of $<0.01^\circ$ of shift/h was observed for intermediate pH, consistent with Mardilovich et al.³²

III. Results and Discussion

1. Detection of a Complete Exchange of Pore Material.

Since the pores are open to the external environment, when the PAA film is immersed in a wetting liquid media, the pores will also be infused with the liquid. We began this experiment by filling the pores with 5 mM PBS (pH 7.4) and then exchanged the PBS with ethanol. $\epsilon_{\text{PBS}} = 1.774$ and $\epsilon_{\text{ethanol}} = 1.845$, thus ϵ_{eff} of the PAA film increased together with the increase in dielectric constant inside the pores. This was detected as

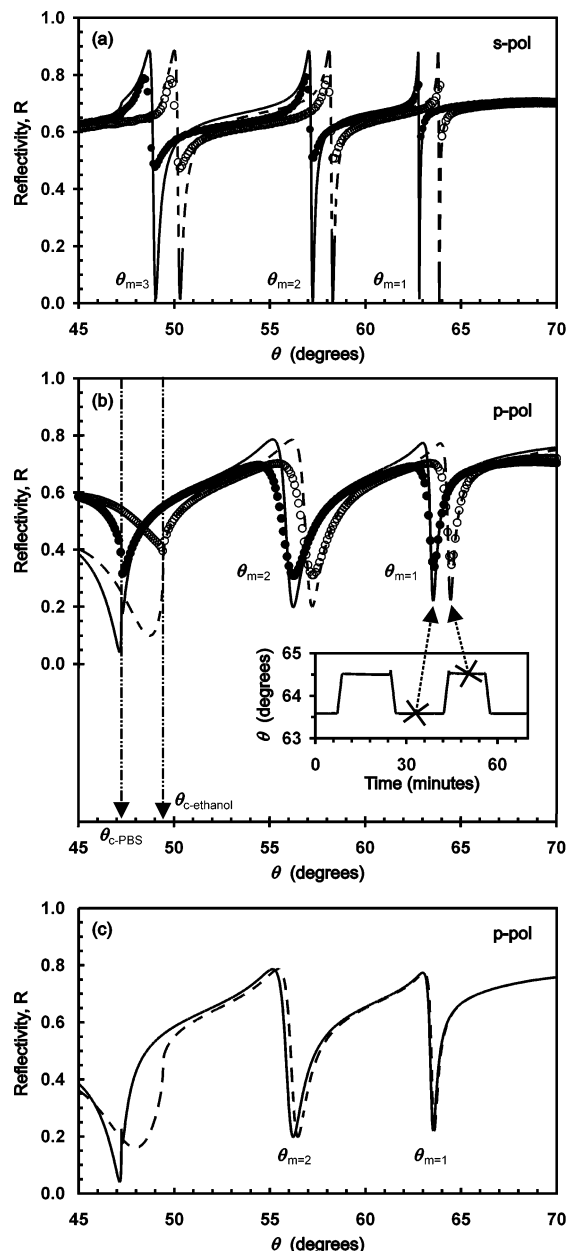


Figure 3. Waveguide mode patterns of PAA film filled with pH 7.4 PBS (filled circles) and ethanol (open circles) under s- (a) and p-polarization (b). Kinetics of the exchange is shown in the inset. Lines fitted to data are the corresponding Fresnel calculations. Parallel shifts in waveguide mode angles are highly characteristic of a change in the effective dielectric constant of the PAA due to an exchange in pore material. Changes in the external media alone produce angle shifts that are larger for higher order modes, simulated in part c. Excitation under s-polarization shows identical behavior. Dielectric constants of the external media are measured independently with $\theta_{c-\text{PBS}}$ and $\theta_{c-\text{ethanol}}$ (c).

approximately parallel shifts in the mode coupling angles to higher values (Figure 3a,b; $\Delta\theta = 0.92^\circ$), which is highly characteristic of a change in ϵ_{eff} . In contrast, a change in the dielectric medium outside the pores alone produces a different pattern of shift, simulated in Figure 3c. Here, ϵ_{eff} remained constant while the dielectric constant outside the pores changed from ϵ_{PBS} to $\epsilon_{\text{ethanol}}$ as if the pores were isolated from the environment. The pattern of angle shifts in this case is characterized by smaller increases in the waveguide coupling angles with higher order modes. In fact, the shift for the $m = 1$ mode is relatively minute due to the change in the cladding medium. There is higher coupling efficiency under p-polariza-

tion, therefore the $m = 1$ mode (p-pol) was chosen for kinetic tracking of changes in the dielectric constant of the porous alumina layer. The exchange between PBS and ethanol in the pores necessarily goes together with an identical change above the film. This change in the surroundings is independently detected as a change in the critical angle for total internal reflection from $\theta_{c\text{-PBS}}$ to $\theta_{c\text{-ethanol}}$ (Figure 3b.) Note that the difference between ϵ_{PBS} and $\epsilon_{\text{ethanol}}$ is a relatively drastic one and we shall demonstrate in the following sections the detection of much smaller changes with the PAA sensor.

The corresponding kinetic measurement is shown in the inset of Figure 3b. Repeated exchanges show identical coupling angle changes and indicate that the PAA film is stable in pH 7.4 PBS and ethanol. In addition to the parallel angle shifts, this repeatability indicates further that the exchanges were complete. (It is highly unlikely that the pores were randomly "half-filled" by the same amount during successive exchanges.) The sloped steps in the inset, however, are due to the finite response time of the instrumentation designed for angular resolution rather than for the relatively large and fast responses shown.

Referring to parts a and b of Figure 3, the fit between data and Fresnel calculations is excellent. As discussed in the Experimental Section, decreases in amplitude and broadening around coupling angle dips compared with the ideal of the simulation are expected, but calculations of the pertinent coupling angles produce exact fits with data. The values of ϵ_{eff} thus obtained are $\epsilon_x = \epsilon_y = 2.317$ and $\epsilon_z = 2.360$ in PBS, and $\epsilon_x = \epsilon_y = 2.347$ and $\epsilon_z = 2.385$ in ethanol. These values are intermediate between those of pure alumina and the respective solutions and it is noted that $\epsilon_z > \epsilon_x, \epsilon_y$. A simple conceptual framework of the dielectric response at pore-alumina boundaries oriented parallel and perpendicular to the incident electric field may suffice to explain this difference: ϵ_{eff} is generally different from a volume-averaged value because screening charge, which depends on the shape and size of inclusions, develops at inclusion-matrix boundaries and sets apart the local and the macroscopic applied fields.¹⁴ The minimum and maximum deviations of ϵ_{eff} from the volume-averaged value are specified by the Wiener bounds:¹⁴

$$\epsilon_{\text{min}} = f_a \epsilon_a + (1 - f_a) \epsilon_b \quad (1)$$

$$1/\epsilon_{\text{max}} = f_a/\epsilon_a + (1 - f_a)/\epsilon_b \quad (2)$$

where f_a is the volume fraction of component a, and $\epsilon_{\text{min}} > \epsilon_{\text{max}}$ for $0 < f_a < 1$. ϵ_{min} is equal to the volume averaged value and is applicable when the local and macroscopic fields are identical everywhere. Such is the case, for example, if all internal boundaries in a laminar composite are parallel to the electric field. In contrast, ϵ_{max} refers to the situation when the electric field has to penetrate the laminae oriented normal to the field direction. In the PAA waveguide, ϵ_x and ϵ_y describe the dielectric responses when an electric field is incident with the plane of the film and, essentially, the field penetrates normal to the cylindrical pore surfaces column after column, similar to the situation for ϵ_{max} . On the other hand, ϵ_z can be compared to ϵ_{min} because ϵ_z describes the response to an electric field normal to the film surface and incident with the straight pores. Thus $\epsilon_{\text{min}} \sim \epsilon_z > \epsilon_{\text{max}} \sim \epsilon_x, \epsilon_y$.

2. Monitoring Pore Widening. Following the previous experiment that left the PAA waveguide immersed in PBS (pH 7.4), we introduced 0.1 M phosphoric acid into the flow cell to initiate pore widening and observed the shift in the $m = 1$ (p-pol) coupling angle. After 25 min, we rinsed the flow cell with PBS pH 7.4 and measured the coupling angles again. Figure 4

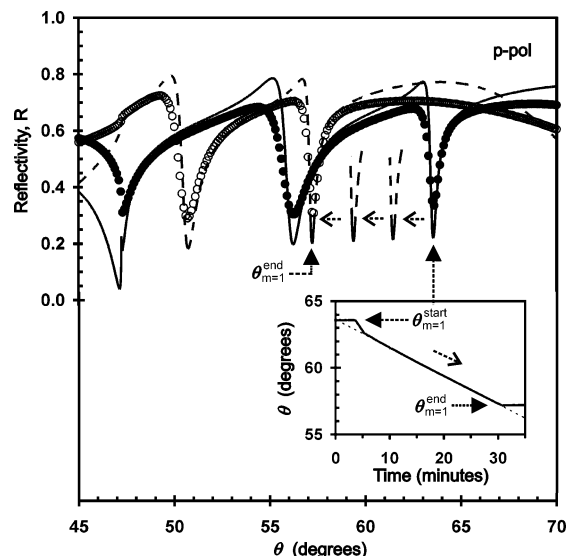


Figure 4. Kinetics of pore widening by phosphoric acid etching. The angle shift and the decrease in the film dielectric constant with time are highly linear except for an initial transient. Dashed curves show Fresnel calculations with dielectric values at equally spaced intervals. The corresponding pore widening is from 41 to 58 nm. Filled circles, measurement before pore widening; open circles, after pore widening.

shows both the kinetic and R vs θ measurements. As expected, the coupling angles were shifted to lower values after pore widening, corresponding to a decrease in the ϵ_{eff} of the PAA film because of a decrease in the volume fraction of alumina: $\epsilon_{\text{alumina}} > \epsilon_{\text{PBS}}$. Although $\epsilon_{\text{alumina}}$ is unknown for the present anodization conditions, it is expected to range between 2.2 (PAA prepared by Hornyak et al.¹) and 3.1 (fully dense film³³). Fresnel fits give $\epsilon_{z\text{-start}} = 2.36$ and $\epsilon_{z\text{-final}} = 2.17$. From measurements of SEM micrographs, the pore diameter increased from ~41 to 58 nm, and the pore volume fraction from 13% to 26%. Fresnel fits also gave a film thickness change from 1150 to 1130 nm, which is comparable to the amount of pore widening. However, the $m = 1$ (p-pol) shift is much more sensitive to a change in ϵ_{eff} than to film thickness, and we do not employ the effects of the film thickness change for sensing purposes.

The inset of Figure 4 also shows that $\Delta\theta_{m=1}$ is linear with the duration of pore widening, except for an initial transient. Moreover, calculations of $\theta_{m=1}$ for equally spaced values of ϵ_{eff} and film thickness between $\epsilon_{z\text{-start}}$ and $\epsilon_{z\text{-final}}$ show that $\Delta\theta_{m=1}$ varies linearly with $\Delta\epsilon_z$ ($R^2 = 0.9999$ for a linear fit.)

With respect to the sensitivity of the PAA sensor, we observe $\theta_{\text{start}} - \theta_{\text{end}} = 6.29^\circ$, while the change in ϵ_z is 0.19, which gives a resolution of $0.03\Delta\epsilon_z/\text{deg}$, or a smallest *experimentally* detectable change of $\Delta\epsilon_z = 2 \times 10^{-4}$, given the 0.005° resolution in the instrumentation. In terms of physical dimensions, with a measured change of 17 nm in pore diameter, we are able to observe changes in average pore diameter of 2.7 nm/deg, which indicates a subangstrom detection of ~0.01 nm. Angle tracking has a virtually unlimited dynamic range, as long as the waveguide mode being tracked is excited. For increased sensitivity but reduced dynamic range, the reflectivity at fixed angles where the R vs θ scan has a high gradient (near the waveguide coupling angles) can be tracked instead. Here the slope in R vs θ is approximately linear and shifts in the coupling angle produce parallel translations of the curve. The change in reflectivity at this fixed angle thus displays a response proportional to the coupling angle shift but multiplied by the slope within the linear region. The practical limit to sensitivity here is the inherent stability of the laser intensity, and the root-mean-

square value of the intensity amplitude is easily $<0.1\%$ in reflectivity. Given the sharpness of the waveguide coupling dips, this would give a sensitivity in dielectric constant $\Delta\epsilon_z \approx 10^{-6}$ and a corresponding increase in the sensitivity in thickness changes. In comparison, an integrated Mach Zehnder interferometer demonstrated detection of a bulk dielectric constant change of $\Delta\epsilon = 9 \times 10^{-6}$ and a layer thickness change of 0.02 nm, which is already at least an order of magnitude better than obtainable with surface plasmon spectroscopy.³⁴ Thus the present configuration is capable of sensitivities at least comparable with integrated optics (IO) devices and surpasses that of surface plasmon spectroscopy (SPS). Naturally, the sensitivity of an optical sensor depends on the optical contrast between the analyte and the background material.

3. BSA Adsorption, Desorption, and Readsorption. BSA is a protein of approximately ellipsoidal dimensions $12 \times 3 \times 3$ nm³.^{24,35} It physisorbs onto various surfaces through a range of mechanisms that include electrostatic interactions,^{25,35} hydrogen bonding,^{26,35} and multipoint interaction with hydrophobic residues.³⁵ The isoelectric point (IEP) of BSA is around pH 5, at which adsorption reaches a maximum,^{21,24,25} regardless of the charge state of the adsorption surface.²¹ (Alumina is an amphoteric oxide and its surface charge is dependent on pH in aqueous solution. IEP for PAA membranes has been measured to be pH ~ 8 ³⁶ and agrees well with pH ~ 9 for α -alumina particles.²¹) Thus the alumina surface for our adsorption experiments from pH 3.8 to 7.4 is always positively charged. Monolayer coverage calculated for BSA varies from 0.4 to 2.4 to 8.5 mg/m², depending on whether there is complete spreading of BSA, or whether its globular conformation is intact and its long axis is perpendicular or parallel to the surface.²⁴ Multilayer adsorption has not been observed in the literature nor in our preliminary experiments (data not shown). Experimentally, the maximum amount of BSA adsorbed on alumina particle surfaces at BSA's IEP ranges from 1.6 mg/m² for protein concentrations $> 17 \mu\text{M}$ ²⁴ to 4.7 mg/m² for protein concentrations $> 30 \mu\text{M}$.²¹ Using a BSA concentration of 50 μM in the present experiment, we expect the maximum amount adsorbed at IEP to be within that range. Desorption is achieved when BSA covered surfaces are exposed to pH conditions far away from the IEP. In terms of kinetics, both adsorption and desorption follow two stages that can be described by two first-order rate equations.^{21–23,30} The initial stages dominate for the first ~ 10 min. The second stage for adsorption is a steady state that continues until equilibrium is reached, while that for desorption is very slow and takes 20 h to reach equilibrium, with residue amounts of BSA still remaining on the surface.

To verify the behavior of the interaction of BSA with the PAA surface, adsorption was carried out over a range of pH values centered around BSA's IEP. Due to the high sensitivity of the sensor, we carried out a series of adsorption–desorption cycles at different pH values with the *same* PAA film to directly compare the adsorbed amount without any possible external influences such as differences in pore sizes or PAA film thickness between samples.

Figure 5 shows the kinetics of one such series of experiments measured by angle tracking of $\Delta\theta_{m=1}$ (p-pol). Adsorption steps were 90 min long while desorption steps lasted 60 min. The pH values shown refer to the adsorption condition while all desorption steps were carried out at pH 8.5. In the first cycle, BSA adsorbed at pH 5 formed a layer of material with $\epsilon_{\text{protein}} = 2.1$ (refractive index = 1.45³⁷) on the pore and film surfaces. This displaced the volume originally occupied by PBS at $\epsilon_{\text{PBS}} = 1.774$ and ϵ_{eff} of the PAA waveguide increased, which is

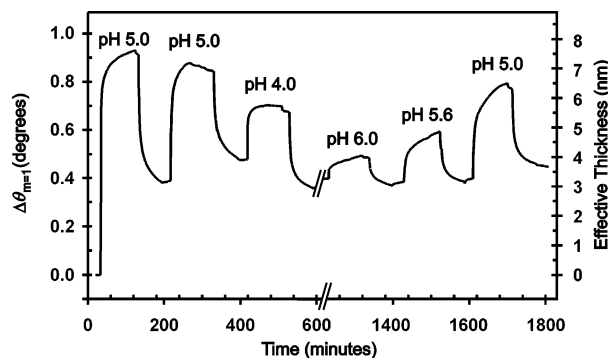


Figure 5. Kinetics of repeated BSA adsorption and desorption. pH values shown refer to those used during adsorption. Note that maximum adsorption is always at the IEP of BSA at pH 5.0. Complete desorption of BSA from alumina is not possible and an apparent baseline for the regenerated alumina surface is established after the first desorption.

reflected as a shift of coupling angles to higher values. As discussed in the last section, there is excellent empirical linearity between $\Delta\theta_{m=1}$ and $\Delta\epsilon_{\text{eff}}$. We have also shown that ϵ_z can be compared to ϵ_{min} in eq 1 and $\Delta\theta_{m=1}$ is therefore linearly related to $\epsilon_a = \epsilon_{\text{pore}}$. The more protein is adsorbed on the pore surface, the higher the ϵ_{pore} is, therefore $\Delta\theta_{m=1}$ corresponds to the amount of BSA adsorbed. Thus Figure 5 shows that BSA adsorption proceeds at a decreasing rate. Given that multilayer BSA adsorption is not expected, we also deduce that $\Delta\theta_{m=1}$ is proportional to the volume-averaged thickness of BSA adsorbed. Similarly, desorption is also shown to proceed at a decreasing rate. These observations are in accordance with the reported adsorption and desorption behavior of BSA interacting with surfaces without confined dimensions and of varying composition.^{21,24–26}

After the first adsorption at pH 5, most of this protein layer was desorbed and subsequent readsorption at the same pH shifted the coupling angle (amount of BSA adsorbed) back to nearly the same level. Figure 6a shows the R vs θ scans obtained on the blank film and after the first readsorption at pH 5. Using eq 1, we estimated the amount of BSA adsorbed. In the film system before adsorption, the dielectric constant in the pores, $\epsilon_{\text{pore}} = \epsilon_{\text{PBS}}$, and the pore volume fraction (f_{pore}) were measured from SEM micrographs. However, the dielectric constant for alumina anodized with our conditions, $\epsilon_{\text{alumina}}$, is unknown. After adsorption, the pores were coated with BSA and ϵ_{pore} increased to an unknown value. Therefore, we obtain ϵ_z from R vs θ scans before and after adsorption and set up two simultaneous equations of eq 1 to solve for both $\epsilon_{\text{alumina}}$ and ϵ_{pore} . Once ϵ_{pore} after adsorption is solved for, using known values of $\epsilon_{\text{PBS}} = 1.774$ and $\epsilon_{\text{protein}} = 2.1$, the volume fraction of protein in the pores is estimated by applying eq 1 to the protein–PBS system within the pores. The effective thickness of BSA deposited on the pore surfaces (h_{BSA}) is then obtained by using this volume fraction and the pore diameter measured from SEM micrographs for this sample (~ 31 nm). A value of $\epsilon_{\text{alumina}} = 2.5$ was obtained from this analysis and is very reasonable for porous anodized alumina.^{1,33} The calculated value of h_{BSA} is shown as the right-hand scale bar in Figure 5. The maximum amount of BSA adsorbed is approximately 7 nm thick and corresponds to a layer of BSA oriented in mixed flat and upright positions. Estimating from the ellipsoidal dimensions of BSA and calculated full monolayer coverage, the maximum h_{BSA} observed is ~ 4.9 mg/m², which is consistent with values reported in the literature for the 50 μM BSA solution used.

The second desorption shown in Figure 5 did not proceed long enough to take the regenerated surface back to the baseline level indicated by the first desorption. However, the third, fourth,

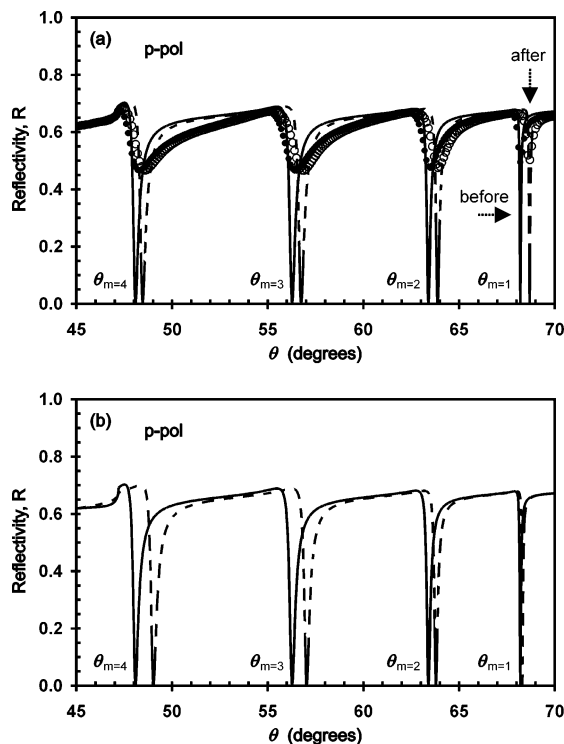


Figure 6. (a) Waveguide mode patterns of blank film (filled circles) and film with BSA readsorbed at pH 5.0 (open circles). BSA adsorption is characterized by parallel shifts in mode coupling angles. (b) Comparison of Fresnel calculations for the same PAA film if a 50-nm protein layer were deposited *above* the film instead of onto the internal pore surfaces. The larger shifts for higher order modes distinguish this external deposition from BSA adsorption into the porous film shown in part a.

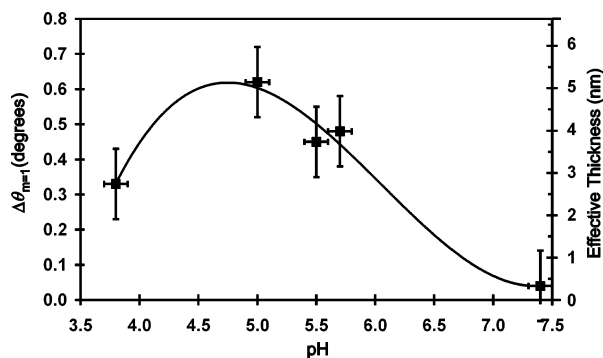


Figure 7. $\Delta\theta_{m=1}$ and thickness of BSA adsorbed of a second sample (pore diameter = 28 nm) plotted as a function of pH. Maximum adsorption at pH 5.0 (IEP of BSA) is characteristic of the protein's physisorption on a range of surfaces, including alumina.

and fifth desorptions all did. We also note that there is a drop in $\Delta\theta$ between the first and last readsorptions at pH 5.0. Subtleties in the kinetics of BSA adsorption and desorption are beyond the scope of the present study, and we take the difference in minimum angles reached as a safe margin of uncertainty for $\Delta\theta$ measured. Even when assuming such large uncertainties, it is seen that maximum BSA adsorption always occurred around the IEP and decreases with pH deviating from the IEP. To confirm this result, a second set of experiments on a different film (pore diameter \sim 28 nm) was carried out with longer desorption cycles such that the regenerated baseline established after the first adsorption—desorption cycle was always reached. Figure 7 summarizes these data and reproduces the pattern of BSA adsorbed vs pH plots seen in the literature on flat and

convex surfaces, which suggests that (bio-) chemically important experiments may be carried out with this PAA sensor.

Parallel shifts in coupling angles shown in Figure 6a indicate that a change in the effective dielectric constant was caused by BSA adsorption—BSA was adsorbed into and throughout the pores. However, could BSA deposition/agglomeration on top of the PAA film account for the angle shifts? First of all, the dielectric constants of both pure and BSA loaded buffers are 1.774 for the low concentrations considered here. Thus only ϵ_{eff} is changed if BSA adsorbed onto pore surfaces. As discussed previously, a change in ϵ_{eff} produces parallel shifts in coupling angles for different waveguide modes. In contrast, if BSA adsorbed or accumulated on top of the PAA film, the coupling angles for higher order modes are shifted much more than the lower order modes: Figure 6b shows Fresnel calculations for a blank PAA film filled with PBS and the same film with a 50 nm protein layer added on top, and demonstrates that appreciable shifts in $\theta_{m=1}$ can only be effected by an improbably thick protein layer (50 nm in Figure 6b, compared with ellipsoidal dimensions of $12 \times 3 \times 3 \text{ nm}^3$ for BSA, which does not form multilayers). Thus the parallel mode angle shifts in Figure 6a confirm BSA adsorption onto pore surfaces. Alternatively, could the shifts be produced by concentrated BSA adsorption down only part of the pores? Again, the best fit between the data and calculations is given by assuming the most straightforward case of adsorption through the length of the pores. In addition, to explain the angle shifts by partial filling of the pores would impose tight restrictions on the distribution of such partial deposition along the length of the pores and is considered unlikely. Thus we conclude that we have demonstrated BSA adsorption on PAA pore surfaces and high sensitivity detection of the protein at the monolayer and submonolayer level.

IV. Conclusions

We have adapted porous anodic alumina (PAA) as a highly sensitive detector of surface reactions and processes by applying it as a planar optical waveguide. Through a simple pore widening experiment, we illustrated how the new sensor can simultaneously assist in nanoscale fabrication processes and monitor the same processes with angstrom level sensitivity. This is also the first time that pore widening has been tracked in situ. In another experiment—BSA adsorption, desorption, and readsorption—we demonstrated kinetic tracking of (bio-) molecular processes, and confirmed that BSA adsorbed onto the porous anodic alumina in a manner analogous to its physisorption on other free surfaces in terms of both kinetics and response to pH environment. High sensitivity is realized by the very large internal surface area of the nanoporous structure, which amplifies the amount of material deposited on the film, and by the minute changes needed to shift waveguide coupling conditions. Although we used prism coupling for guiding light into the PAA film, grating or end-fire coupling and channel waveguide configurations can also be envisioned.

The sensitivity to thickness changes is on the subangstrom level and corresponds to $\Delta\epsilon = 10^{-4}$ in the effective dielectric constant of the PAA film. A simple switch in the experimental setup to observing angle shift through reflected intensity change would increase the sensitivity to $\Delta\epsilon = 10^{-6}$. Further increases in sensitivity may be achieved by fine-tuning the PAA fabrication conditions to improve film uniformity and to increase the pore density (leading to an increase in internal surface area for reactions to take place).

The examples presented show that anodic alumina films can be employed as a highly sensitive device to monitor processes

occurring within the alumina pores in situ. These processes may be related to the use of anodic alumina in nanotechnology as a template or scaffold, or they may be related to other surface reactions and processes. Indeed the present experiments only minimally illustrate the full potential of the PAA sensor. One important omission is in functionalization of the alumina surface through silane-coupled molecules for specific molecular interaction and detection. Analogous to the physisorption of a BSA monolayer, growth of a self-assembled monolayer (SAM) can be monitored as an average layer thickness change. Reactions that are specific toward alumina surfaces may also be of interest, and target molecules tagged with fluorophores may be employed concurrently with fluorescence microscopy for multitarget, high-resolution detection.

Acknowledgment. We thank Bernhard Menges at the Max Planck Institute for Polymer Research, Mainz, and Xiaodi Su at the Institute of Materials Engineering and Research, Singapore, for their excellent input concerning Fresnel modeling of anisotropic films and protein properties, respectively. Part of this material is based upon work supported by the Science and Engineering Research Council, Singapore, under grants R-152-000-037-303 (A*Star) and R-152-000-037-112 (MOE).

References and Notes

- (1) Hornyak, G. L.; Patrissi, C. J.; Martin, C. R. *J. Phys. Chem. B* **1997**, *101*, 1548–1555.
- (2) Hoyer, P. *Adv. Mater.* **1996**, *8*, 857.
- (3) Sander, M. S.; Tan, L. S. *Adv. Funct. Mater.* **2003**, *13*, 393–397.
- (4) Martin, C. R. *Chem. Mater.* **1996**, *8*, 1739–1746.
- (5) Black, M. R.; Padi, M.; Cronin, S. B.; Lin, Y. M.; Rabin, O.; McClure, T.; Dresselhaus, G.; Hagelstein, P. L.; Dresselhaus, M. S. *Appl. Phys. Lett.* **2000**, *77*, 4142–4144.
- (6) Proux-Delrouyre, V.; Elie, C.; Laval, J.-M.; Moiroux, J.; Bourdillon, C. *Langmuir* **2002**, *18*, 3263–3272.
- (7) Hennesthal, C.; Steinem, C. *J. Am. Chem. Soc.* **2000**, *122*, 8085–8086.
- (8) Routkevitch, D.; Govyadinov, A. N.; Mardilovich, P. P. *Micro-Electro-Mech. Syst. (MEMS)* **2000**, *2*, 39–44.
- (9) Masuda, H.; Satoh, M. *Jpn. J. Appl. Phys.* **2** **1996**, *35*, L126–L129.
- (10) Masuda, H.; Yamada, H.; Satoh, M.; Asoh, H.; Nakao, M.; Tamamura, T. *Appl. Phys. Lett.* **1997**, *71*, 2770–2772.
- (11) O'Sullivan, J. P.; Wood, G. C. *Proc. R. Soc. London Ser. A* **1970**, *317*, 511–543.
- (12) Li, F.; Zhang, L.; Metzger, R. M. *Chem. Mater.* **1998**, *10*, 2410–2480.
- (13) Baselt, D. R.; Lee, G. U.; Hansen, K. M.; Chrisey, L. A.; Colton, R. J. *Proc. Inst. Electr. Electron. Eng.* **1997**, *85*, 672–680.
- (14) Aspnes, D. E. *Thin Solid Films* **1982**, *89*, 249–262.
- (15) Granqvist, C. G.; Hunderi, O. *Phys. Rev. B* **1978**, *18*, 2897–2905.
- (16) Foss, C. A., Jr.; Hornyak, G. L.; Stocket, J. A.; Martin, C. R. *J. Phys. Chem.* **1994**, *98*, 2963–2971.
- (17) Saito, M.; Shibasaki, M.; Nakamura, S.; Miyagi, M. *Opt. Lett.* **1994**, *19*, 710–712.
- (18) Knoll, W. *Annu. Rev. Phys. Chem.* **1998**, *49*, 569–638.
- (19) Elam, J. W.; Routkevitch, D.; Mardilovich, P. P.; George, S. M. *Chem. Mater.* **2003**, *15*, 3507–3517.
- (20) Liang, Z. J.; Susa, A. S.; Yu, A. M.; Caruso, F. *Adv. Mater.* **2003**, *15*, 1849–1853.
- (21) Fukuzaki, S.; Urano, H.; Nagata, K. *J. Ferment. Bioeng.* **1996**, *81*, 163–167.
- (22) Urano, H.; Fukuzaki, S. *J. Colloid Interface Sci.* **2002**, *252*, 284–289.
- (23) Sarkar, D.; Chattoraj, D. K. *Ind. J. Biochem. Biophys.* **1992**, *29*, 135–142.
- (24) Hajra, S.; Chattoraj, D. K. *Ind. J. Biochem. Biophys.* **1991**, *28*, 114–123.
- (25) Elgersma, A. V.; Zsom, R. L. J.; Lyklema, J.; Norde, W. *Colloids Surf.* **1992**, *65*, 17–28.
- (26) Silin, V.; Weetall, H.; Vanderah, D. J. *J. Colloid Interface Sci.* **1997**, *185*, 94–103.
- (27) Lawall, R.; Knoll, W. *J. Appl. Phys.* **1994**, *76*, 5764–5768.
- (28) Hickel, W.; Duda, G.; Jurich, M.; Kroehl, T.; Rochford, K.; Stegeman, G. I.; Swalen, J. D.; Wegner, G.; Knoll, W. *Langmuir* **1990**, *6*, 1403–1407.
- (29) Mardilovich, P. P.; Govyadinov, A. N.; Mukhurov, N. I.; Rzhetskii, A. M.; Paterson, R. *J. Membr. Sci.* **1995**, *98*, 131–142.
- (30) Sarkar, D.; Chattoraj, D. K. *J. Colloid Interface Sci.* **1996**, *178*, 606–613.
- (31) Pouliot, M.; Pouliot, Y.; Britten, M.; Ross, N. *J. Membr. Sci.* **1994**, *95*, 125–134.
- (32) Mardilovich, P. P.; Govyadinov, A. N.; Mazurenko, N. I.; Paterson, R. *J. Membr. Sci.* **1995**, *98*, 143–155.
- (33) *Handbook of Optical Constants of Solids*; Palik, E. D., Ed.; Academic Press: San Diego, CA, 1998; Vol. 3.
- (34) Weisser, M.; Tovar, G.; Mittler-Neher, S.; Knoll, W.; Brosinger, F.; Freimuth, H.; Lacher, M.; Ehrfeld, W. *Biosens. Bioelectron.* **1999**, *14*, 405–411.
- (35) Urano, H.; Fukuzaki, S. *J. Biosci. Bioeng.* **2000**, *90*, 105–111.
- (36) Winkler, B. H.; Baltus, R. E. *J. Membr. Sci.* **2003**, *226*, 75–84.
- (37) Spinke, J.; Liley, M.; Schmitt, J.; Guder, H. J.; Angermaier, L.; Knoll, W. *J. Chem. Phys.* **1993**, *99*, 7012–7019.